ACS OMEGA

Open Access

http://pubs.acs.org/journal/acsodf

Article

Crystals of Diphenyl-Benzothiadiazole and Its Derivative with Terminal Trimethylsilyl Substituents: Growth from Solutions, Structure, and Fluorescence Properties

Valery A. Postnikov,* Nataliya I. Sorokina, Artem A. Kulishov, Georgy A. Yurasik, Timofei A. Sorokin, Maria S. Lyasnikova, Oleg V. Borshchev, Maxim S. Skorotetcky, Sergey A. Pisarev, Evgeniya A. Svidchenko, Nikolay M. Surin, and Sergey A. Ponomarenko*

Cite This: *ACS Omega* 2024, 9, 14932−14946

Read Online

ACCESS | Metrics & More | Article Recommendations | Supporting Information

ABSTRACT: Linear conjugated molecules consisting of benzothiadiazole (BTD) and phenyl rings are highly efficient organic luminophores. Crystals based on these compounds have great potential for use as light-emitting elements, in particular, scintillation detectors. This paper compares the peculiarities of growth, structure, and fluorescent properties of crystals based on 4,7-diphenyl-2,1,3-benzothiadiazole (**P_2-BTD**) and its organosilicon derivative 4,7-bis(4-(trimethylsilyl)phenyl) BTD (**(TMS-P)$_2$-BTD**). The conditions for the formation of centimeter-scale single crystals were found for the former, while it was possible to prepare also bulky faceted individual crystals for the latter. The structures of **P_2-BTD** and **(TMS-P)$_2$-BTD** crystals at 85 and 293 K were investigated by single-crystal X-ray diffraction. The crystal structure of **P_2-BTD** has been refined (sp. gr. $P\bar{1}$, $Z = 4$), and for **(TMS-P)$_2$-BTD** crystals, the structure has been solved for the first time (sp. gr. $P2_1/c$, $Z = 32$). Experimental and theoretical investigations of the absorption-fluorescent properties of solutions and crystals of the molecules have been carried out. The luminophores are characterized by a large Stokes shift for both solutions and crystals with a high fluorescence quantum yield of 75−98% for solutions and 50−85% for the crystals. A solvatochromic effect was observed for solutions of both luminophores: an increase in the values of the fluorescence quantum yield and the excited state lifetime were established with increasing the solvent polarity. Fluorescence properties of solutions and crystals have been analyzed using the data on crystal structure and conformation structure of the molecules as well as density functional theory calculations of their electronic structure. The results have shown that the crystal packing of **P_2-BTD** molecules exhibits uniformity in conformational states, while **(TMS-P)$_2$-BTD** molecules display a variety of conformational structures in the crystals. This unique combination of features makes them a remarkable example among the other molecular systems for identifying the relationship between the structure and absorption-fluorescence properties through comparative analysis.

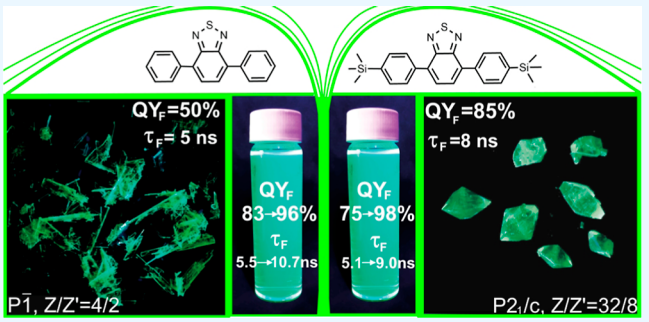

INTRODUCTION

Linear conjugated molecules with a central benzothiadiazole (**BTD**) fragment are well-known as stable organic luminophores with a large Stokes shift and high fluorescence quantum yield.[1−4] Crystals based on these compounds, due to a wide range of remarkable properties, are attractive for the development of optoelectronic technologies based on them.[5−7] Of great interest are well-crystallized substances capable of forming large single crystals with a size of the order of 1 cm or more, which is a huge advantage for a detailed study of the relationship between their structure and properties and has high potential for their application as optical single crystal elements obtained by growth methods from solutions or melt. Good candidates for this task are rather short linear conjugated molecules with a sufficiently high solubility in standard organic solvents as well as stable over a wide operating temperature range. It should be noted that crystallization of the molecules with a central **BTD** fragment is still scarcely studied in the literature,[8,9] and there are no data on the growth of bulk single crystals at a scale of ∼1 cm.

A molecule of 4,7-diphenyl-2,1,3-benzothiadiazole (**P_2-BTD**), consisting of two phenyl groups symmetrically conjugated in the 4- and 7-positions position with the central

Received: October 29, 2023
Revised: February 26, 2024
Accepted: March 4, 2024
Published: March 21, 2024

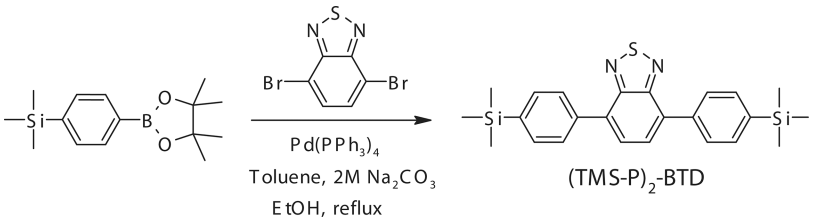

Figure 1. Scheme for the synthesis of **(TMS-P)$_2$-BTD**.

BTD fragment, is a good base for obtaining a whole family of its derivatives with unique optical properties.[2,3,5,7,10,11] This compound itself is also promising as a highly efficient luminophore, for example, for use as luminescent labels or the development of a scintillation detector. Compared to *para*-terphenyl, the emission spectrum of **P$_2$-BTD** is significantly red-shifted, while the fluorescence quantum yield is similar for both molecules (80−90%).[12,13] The structure of **P$_2$-BTD** single crystals was previously studied at 123[13−15] and 100 K,[3] but the data published are contradictory. Moreover, the features of **P$_2$-BTD** crystallization have not been described, and, in general, the physicochemical properties of crystals of this compound remain poorly understood.

Earlier, by studying the crystallization of novel derivatives of linear conjugated molecules with various terminal substituents, it was found that the presence of trimethylsilyl end groups leads to a significant increase in the solubility of the compound, and, in some cases, contributes to a noticeable improvement in the growth characteristics and quality of the crystals grown from solutions.[16−18]

This work is devoted to investigation of the growth and structure of crystals, and the absorption-fluorescence properties of solutions and crystals of **P$_2$-BTD** and its derivative with terminal trimethylsilyl substituents −4,7-bis((4-trimethylsilyl)-phenyl)BTD (**(TMS-P)2-BTD**) (Figure 1).

EXPERIMENTAL DETAILS

Materials and Methods. All commercially available compounds were purchased from Sigma-Aldrich, Acros organics, or ABCR GmbH and used as received. All solvents used were qualified for spectroscopy. In the case of column chromatography, silica gel 60 "Merck" (Germany) was taken. For thin-layer chromatography, "Sorbfil" (Russia) plates were used. 4,7-Diphenyl-2,1,3-benzothiadiazole (**P$_2$-BTD**) was synthesized as described earlier via Suzuki−Miyaura coupling between 2,1,3-benzothiadiazole and phenylboric acid.[19]

Characterization. The ^{1}H NMR spectra were recorded on a Bruker WP250 SY spectrometer (250.13 MHz) using the residual signal of $CDCl_3$ (δ 7.27 ppm) as the internal standard. The ^{13}C and ^{29}Si NMR spectra were recorded on a Bruker ADVANCE II 300 spectrometer at working frequencies of 75 and 60 MHz, respectively. The spectra were then processed on the computer using the ACD Laboratories software.

Gel permeation chromatography analysis was performed on a Shimadzu instrument with a SPD-M10A^{VP} diode matrix as detector using 7.8 × 300 mm^2 Phenomenex columns (USA) filled with the Phenogel sorbent with a pore size of 500 Å and tetrahydrofuran (THF) as the eluent.

Elemental analysis of C, H, N elements was carried out using a CHN automatic analyzer CE1106 (Italy). The experimental error was 0.30−0.50%. The burning was done in a Sheninger flask using an alkaline solution of hydrogen peroxide as an absorbent.

Infrared spectra were registered with a Bruker Tensor 27 spectrometer.

High-resolution mass spectra were recorded on a Bruker micrOTOF II instrument using electrospray ionization. The measurements were performed in positive ion mode (interface capillary voltage −4500 V); mass range from m/z 50 to m/z 3000 Da; external calibration with Electrospray Calibrant Solution.

Synthesis. The synthesis of 4,7-*bis*[4-(trimethylsilyl)-phenyl]-2,1,3-benzothiadiazole **(TMS-P)$_2$-BTD** was carried out as follows (see Figure 1). A flask was charged with organoboron precursor 4,4,5,5-tetramethyl-2-[4-(trimethylsilyl)phenyl]-1,3,2-dioxaborolane[20] (1.00 g, 3.6 mmol), 4,7-dibromo-2,1,3-benzothiadiazole (480 mg, 1.6 mmol), and $Pd(PPh_3)_4$ (42 mg, 1 mol %). The mixture was degassed, toluene, an aqueous solution of Na_2CO_3 (2.0 M), and ethanol were added and heated to reflux for 14 h. After completion of the reaction, the mixture was cooled down to room temperature, the bottom aqueous phase was removed, and the organic phase was evaporated by a Rotorvapor. The crude product was purified by column chromatography on silica gel from a toluene-hexane (1:3) mixture to give pure **(TMS-P)$_2$-BTD** as a yellowish-green solid (601 mg, 85.2%). ^{1}H NMR (J Hz, $CDCl_3$): δ [ppm] 0.33 (18H, s), 7.72 (4H, d, J = 8.24), 7.79 (2H, s), 7.93 (4H, d, J = 8.24) (Figure S1). ^{13}C NMR ($CDCl_3$): δ [ppm] −1.06; 128.14; 128.51; 133.46; 133.69; 137.80; 140.82; 154.15. ^{29}Si NMR ($CDCl_3$): δ [ppm] −3.77. Anal. Calcd for $C_{24}H_{28}N_2SSi_2$%: C 66.61, H 6.52, N 6.47, S 7.41, Si 12.98. Found,%: C 66.54, H 6.37, N 6.14, S 7.55. Fourier transform infrared (KBr): $\bar{\nu}$ = 3060, 3034, 1549, 1474, 1448 cm^{-1}. HR/MS calcd for $C_{24}H_{28}N_2SSi_2$ [M + H] 433.1584, found 433.1585.

Differential Scanning Calorimetry and Thermogravimetric Analysis. The thermal properties of the compounds were studied in the temperature range from 293 to 770 K in aluminum crucibles by the method of simultaneous thermal analysis; the heat flux [differential scanning calorimetry (DSC)] and mass loss [Thermogravimetric Analysis (TGA)] were simultaneously measured on an STA 449 F1 Jupiter (NETZSCH, Germany) thermoanalytical complex. The experiments were carried out on samples of polycrystalline powders in a dry argon flow of 70 mL/min and at a heating and cooling rate of 5 K/min.

Solubility. The concentration of saturated solutions of the compounds in *n*-hexane was measured spectrophotometrically.[21] The solutions were kept for 24 h over the crystalline precipitate formed at a temperature of 303 K, filtered through poly(tetrafluoroethylene) (PTFE) filters (0.22 μm), and diluted a known number of times so that the optical density did not exceed 0.6 at long-wavelength maxima. The absorption spectra of solutions were measured on a UV-2501PC spectrophotometer (Shimadzu, Japan) in standard quartz cuvettes with a 10 mm optical path.

https://doi.org/10.1021/acsomega.3c08543
ACS Omega 2024, 9, 14932−14946

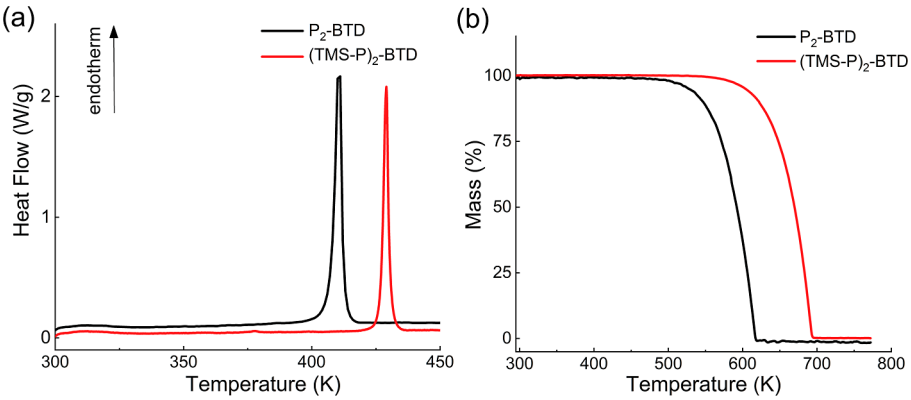

Figure 2. DSC (a) and TGA (b) curves of **P_2-BTD** and **$(TMS\text{-}P)_2$-BTD**.

Crystal Growth and Analysis. Crystal growth was carried out by the method of isothermal evaporation of the solvent at room temperature.[8] *n*-Hexane was used as a solvent. The initial concentrations of the substances in the solutions prepared for growth were 10.4 mM/L for **P_2-BTD** and 16.2 mM/L for **$(TMS\text{-}P)_2$-BTD**. The surface morphology and thickness of the crystals were studied using a LEXT OLS 3100 confocal microscope (Olympus, Japan) and an Ntegra atomic force microscope (NT-MDT, Russia) in contact mode according to the method described earlier.[21] The AFM topograms obtained were processed and analyzed using the Gwyddion program.[22]

X-ray Diffraction. The intensities of diffraction reflections from single crystals **P_2-BTD** and **$(TMS\text{-}P)_2$-BTD** were measured at temperatures of 293 and 85 K on an X-ray diffractometer XtaLAB Synergy-DW, HyPix-Arc 150 (Rigaku Oxford Diffraction). Experimental data were processed using the CrysAlisPro program.[23] Crystallographic calculations (correction for anomalous scattering, allowance for absorption, averaging of reflections equivalent in symmetry) were carried out using the JANA2006 software package.[24] The coordinates of silicon, sulfur, nitrogen, and carbon atoms were found by the charge flipping method using the Superflip program.[25] For **P_2-BTD** single crystals, the analysis of maps of electron density difference syntheses plotted in the vicinity of the positions of carbon atoms revealed peaks of the residual electron density with a height of about 2 e/Å^3 at the distances from 0.7 to 1.2 Å from carbon atoms. In these positions, 12 hydrogen atoms were localized. The coordinates of all atoms in the structure and the parameters of their thermal displacements were refined by the least-squares method in the full matrix version. In the **$(TMS\text{-}P)_2$-BTD** structure model, the coordinates of hydrogen atoms were fixed geometrically. The crystal structure was visualized using the Mercury software package[26] The calculation of the potentials of pair interactions between the nearest molecules in a crystal at 85 K was performed in the force field approximation using the "UNI Intermolecular Potentials" component,[27] which is included in the Mercury package.

Absorption and Fluorescence Spectra. The absorption spectra of molecular solutions in solvents were measured on a UV-2501PC spectrophotometer (Shimadzu, Japan). Fluorescence spectra were measured on an ALS-1 M spectrofluorimeter (ISPM RAS, Moscow, Russia) in photon counting mode at successive time intervals and on a FLUORAN-2 pulsed spectrophotometer-spectrofluorimeter (VNIIOFI, Moscow, Russia). When measuring the fluorescence spectra of solutions, standard 10 × 10 mm quartz cells were used. The fluorescence quantum yield of solutions was determined by comparison with the known quantum yield of standards using the method of measuring the fluorescence of optically diluted solutions.[28] Solutions of rhodamine 6G in ethanol (Φ_F = 0.95) and POPOP in cyclohexane (Φ_F = 0.93) were used as standards for measuring the fluorescence quantum yield of luminophores.[29] Measurements of the quantum yield and fluorescence spectra of crystalline layers deposited on quartz substrates were carried out in an integrating sphere made of highly reflective PTFE. The sphere was calibrated using the fluorescence of a crystalline layer of tetraphenylbutadiene, which is characterized by a high fluorescence quantum yield (Φ_F = 0.95) and low reabsorption losses (k_{reabs} = 0.88).[30,31]

Fluorescence Lifetime Measurements. Fluorescence decay kinetics of solutions and crystals was studied using a FluoTime 300 time-correlated photon counting spectrofluorimeter (PicoQuant, Germany). Fluorescence spectra were obtained by excitation at a wavelength λ_{ex} = 375 ± 2 nm (laser diode source LDH 375). The signal was recorded near the maximum of the fluorescence spectra.

Quantum Chemical Calculations. Calculations of the electronic structure of the compounds were performed using the version 5 of ORCA package[32] in the PBE0 approximation[33] and the 6-31G(d,p) basis set.[34,35]

RESULTS AND DISCUSSION

Differential Scanning Calorimetry and Thermogravimetric Analysis. The DSC curves in the heating scan, which characterize the melting processes of **P_2-BTD** and **$(TMS\text{-}P)_2$-BTD** samples, are shown in Figure 2a (see also Figure S2 in the Supporting Information for the first heating, cooling, and the second heating scans). From the melting peaks of these compounds, the temperatures T_m and molar enthalpies ΔH_m of melting were determined, which are given in Table 1. As can

Table 1. Solubility C_0 in *n*-Hexane (303 K) and Parameters of Melting and Thermostability of P_2-BTD and $(TMS\text{-}P)_2$-BTD[a]

compound	M (g/mol)	T_m (K)	ΔH_m (kJ/mol)	$T_{5\%}$ (K)	C_0 (mM)
P_2-BTD	288.4	407	27	533	30
$(TMS\text{-}P)_2$-BTD	432.7	425	32	603	68

[a] T_m and ΔH_m are temperature and molar enthalpy of melting, respectively, $T_{5\%}$ is the temperature at which the sample loses 5% of its mass.

https://doi.org/10.1021/acsomega.3c08543
ACS Omega 2024, 9, 14932−14946

be seen from Figure 2a, when heated to the corresponding melting temperatures, the luminophores have no polymorphic transitions. For **P_2-BTD**, the melting temperature turned out to be somewhat higher than the value presented in the literature[12] (400−402 K). The melting point of **$(TMS\text{-}P)_2$-BTD** is 18° higher and the molar enthalpy of melting is almost 25% lower than that of **P_2-BTD** (Table 1). Upon repeated thermal cycling, the melting parameters for the compounds investigated are well reproduced (see Figure S2 in the Supporting Information). The compounds exhibit high phase stability with respect to evaporation of the substance even during the transition to a liquid state. As follows from the TGA curves shown in Figure 2b, the compounds evaporate completely without decomposition when heated to high temperatures. A noticeable mass loss (>5%) due to melt evaporation for **P_2-BTD** is observed when heated above 533 K, and for **$(TMS\text{-}P)_2$-BTD**, an equivalent fraction of the sample evaporates at the temperature above 603 K (Figure 2b).

Solubility, Growth, and Surface Micromorphology of Crystals. The values of solubility in *n*-hexane (C_0) determined by the spectrophotometric method at 303 K for the luminophores are presented in Table 1. As can be seen, the concentration of **$(TMP)_2$-BTD** molecules in saturated solution is more than 2 times higher than that of **P_2-BTD**.

From the solution of *n*-hexane, **P_2-BTD** crystals grew in the form of both needles and elongated plates, which represent the same polymorphic form. Figure 3a shows **P_2-BTD** crystals

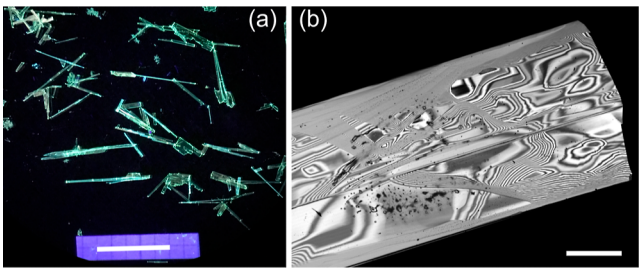

Figure 3. Optical images of **P_2-BTD** crystals: (a) a number of crystals under UV illumination (scale 5 mm). (b) Enlarged confocal image of a developed crystal face (scale 0.1 mm).

grown for 7 days, the largest of which reached a length of 13 mm and a thickness of about 200 μm (see Figures 3a and S3a in the Supporting Information). On the developed surface of elongated crystals, smooth areas with dislocation growth hillocks are observed (Figure 3b). Many crystals show a longitudinal inhomogeneous texture (see Figure S3b in the Supporting Information).

$(TMS\text{-}P)_2$-BTD crystals are typically formed as needles or rods, reaching sizes of 10 mm × 0.5 mm × 0.5 mm over a period of 7 to 14 days (see Figures 4a and S4a in the Supporting Information). The lateral surface of the needle crystals is well faceted (Figure S4a in the Supporting Information). Rarely, the growth of convex faceted crystals was observed in the solution (see Figures 4b and S4b in the Supporting Information). Figure 4b shows **$(TMS\text{-}P)_2$-BTD** crystals grown for 12 days. The largest of the presented crystals has dimensions of 4 mm × 3 mm × 2.5 mm. The surface of the facets of convex crystals is usually rough (see Figures S4c,d in the Supporting Information).

Figure 5 shows AFM images of the surface areas of the developed face of needle crystals **P_2-BTD** (a) and **$(TMS\text{-}P)_2$-BTD** (b). The white arrows indicate orientation of the crystals relative to the image. Series of elementary growth steps 1.5 ± 0.2 nm high for **P_2-BTD** and 0.8 ± 0.2 nm high for **$(TMS\text{-}P)_2$-BTD** were fixed on the surface of the crystals investigated.

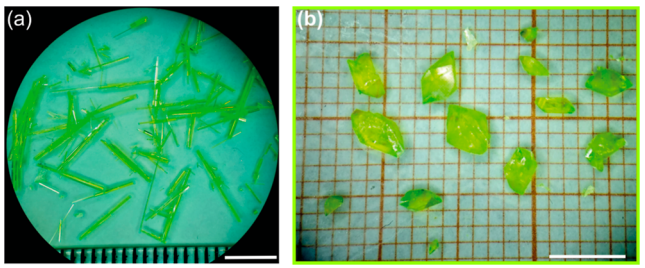

Figure 4. Optical images of **$(TMS\text{-}P)_2$-BTD** crystals in the form of needles (a) and convex polyhedra (b) (scale 5 mm).

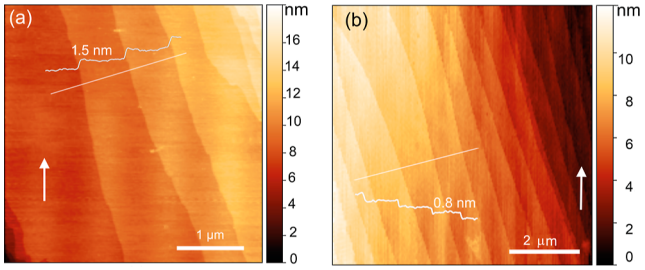

Figure 5. AFM images of the developed face areas of crystals of **P_2-BTD** (a) and **$(TMS\text{-}P)_2$-BTD** (b).

Crystal Structure. The main crystallographic parameters, experimental data, and the results of structure refinement of **P_2-BTD** single crystals at 293 and 85 K and **$(TMS\text{-}P)_2$-BTD** single crystals at 85 K are presented in Table S1 in the Supporting Information. Information about the structure has been deposited in the Cambridge Structural Database (CCDC## 2253931, 2253932, 2300626).

The structure of **P_2-BTD** single crystals was studied earlier at temperatures of 123 K[13−15] and 100 K.[3] It has been established that **P_2-BTD** single crystals at a temperature of 123 K exist in two polymorphic modifications: triclinic[14,15] and monoclinic.[13]

The search for unit cells of crystals in this work ended with the choice of a triclinic cell (sp. gr. $P\bar{1}$) for a **P_2-BTD** single crystal with the parameters indicated in Table S1. Thus, no structural phase transition was revealed for a **P_2-BTD** single crystal with decreasing temperature. The unit cell parameters of the triclinic modification for **P_2-BTD** agree with the values obtained at 100 K in the literature.[3]

$(TMS\text{-}P)_2$-BTD single crystals crystallize in a monoclinic cell (sp. gr. $P2_1/c$) with parameters: a = 23.3432(2), b = 20.7454(1), c = 23.0047(2) Å, β = 118.2953 (6) ° at 293 K, and at 85 K with the parameters indicated in Table S1. It should be noted that it was possible to obtain a model of the structure of **$(TMS\text{-}P)_2$-BTD** single crystals only in a large cell using experimental data measured at 85 K.

The unit cell model of the **P_2-BTD** crystal is shown in Figure 6a. There are 4 molecules in a cell. The presence of a central **BTD** fragment in the molecule leads to the absence of an inversion center in the molecular symmetry. The conformation of the molecule in the crystal is not planar: the phenyl groups are turned relative to the **BTD** fragment in one direction, and the most symmetrical form of the molecule will be characterized by the point group C_S (the presence of a

https://doi.org/10.1021/acsomega.3c08543
ACS Omega 2024, 9, 14932−14946

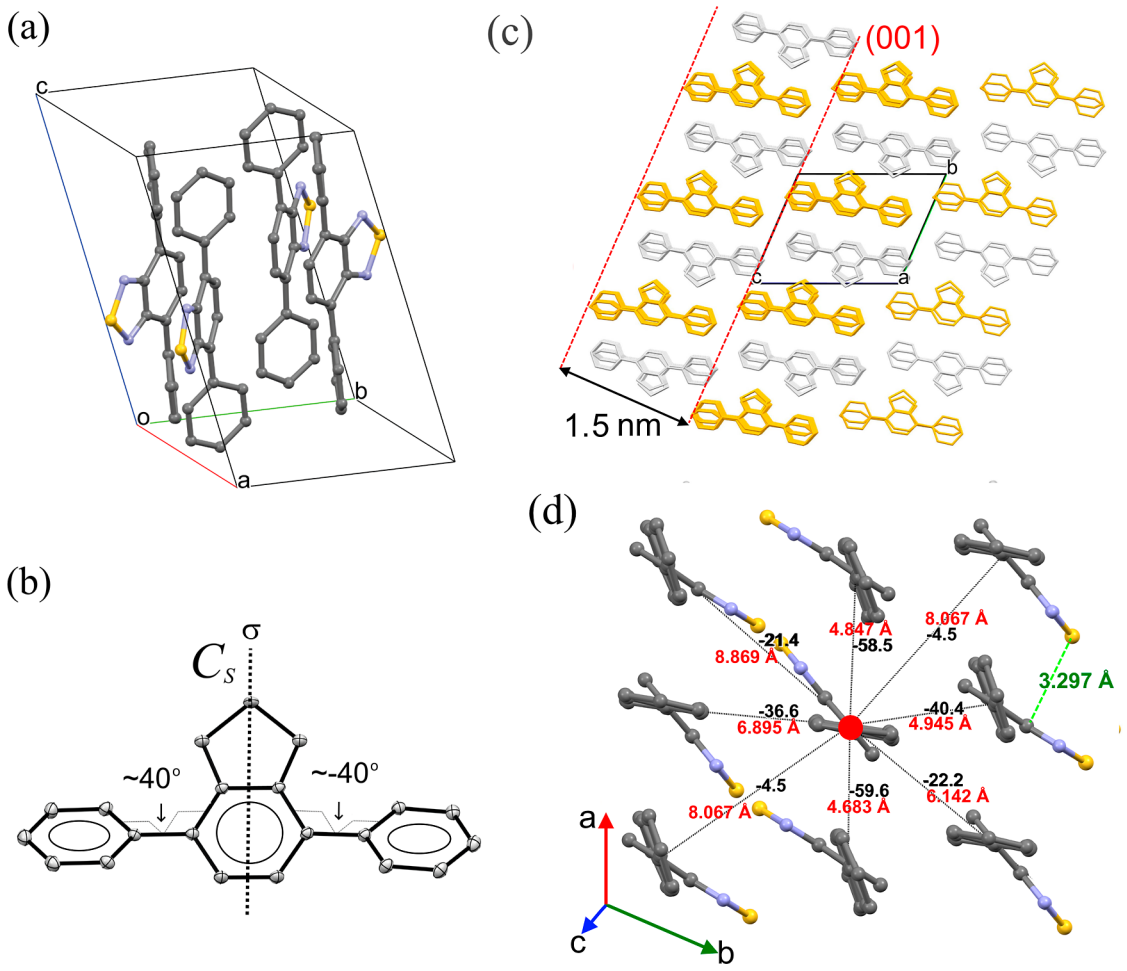

Figure 6. Crystal structure of **P_2-BTD** at 85 K: (a) view of the unit cell. (b) Conformational structure of the molecule in the crystal with the values of torsional angles in the ORTEP representation (thermal ellipsoids with a probability of 50%). (c) Projection of the structure onto the (100) plane. (d) Scheme of lateral intermolecular interactions for nearest neighbors inside the monolayer in the (001) plane orientation, indicating the values of pair potentials in kJ/mol (black numbers) and the distances between the centers of the corresponding molecules.

mirror plane σ) (Figure 6b). In the unit cell, the molecules have torsional angles between the phenyl groups and the central **BTD** fragment in the range of $|40 \pm 4|$ degrees (Figure 6b). A similar feature of the position relative to each other of the central **BTD** fragment and adjacent phenyl groups (torsional angles of about 40°) was previously noted for the molecules of a linear phenyloxazole-benzothiadiazole luminophore in a crystal.[9]

In the crystal structure, monolayers with a thickness of 1.5 nm can be distinguished, which are equivalent in terms of translational symmetry along the *c* axis, parallel to the (001) plane (Figure 6c). These monolayers consist of two subsystems of the densest molecular rows slightly displaced relative to each other along the *c* axis, oriented in the direction of the *a* axis (in Figure 6c, the densest rows of molecules in the projection onto the drawing plane are highlighted in gray and yellow). In the projection onto the (100) plane, the densest rows of molecules form a "brickwork" structure (Figure 6c), which, as a rule, is a characteristic feature for linear conjugated molecules with 1D anisotropic crystal growth.[8,9] In such cases, the crystal growth rate is maximal in the direction close to the direction of the densest rows, within which the strongest interactions take place between the nearest molecules (Figure S5a).

Figure 6d shows a monolayer element in the (001) plane orientation, consisting of molecules of the first coordination circle, for which the values of the potentials of pair interactions (black numbers in units of kJ/mol) with the central molecule and the distances between the centers of the corresponding molecules are indicated. The strongest interaction between the nearest molecules takes place in the [100] direction (−59.6 kJ/mol, 4.7 Å) and the weakest in the [110] direction (−4.5 kJ/mol, 8.0 Å). In the densest [100] rows, the shortest distance between BTD groups of neighboring molecules is about 3.3 Å (Figure 6d). The interaction force between the nearest **P_2-BTD** molecules in the direction of the end contacts (along the *c* axis) is an order of magnitude weaker than in the lateral directions. That is why the surface energy of the (001) face will apparently be the lowest in the crystal system and during its growth, according to the Gibbs-Curie-Wulf theorem, this facet on the side surface of the crystal will be the most developed[36] (see Figure S5a in the Supporting Information). In this regard, the observed elementary growth steps on the surface of the developed face of a **P_2-BTD** crystal (Figure 5a) correspond to the thickness of the monolayers in the (001) plane orientation (Figure 6c).

Compared to the **P_2-BTD** crystal, a unit cell of **(TMS-P)$_2$-BTD** crystal, consisting of 32 molecules, has a more complex structure. The projection of the unit cell onto the (010) plane

https://doi.org/10.1021/acsomega.3c08543
ACS Omega 2024, 9, 14932−14946

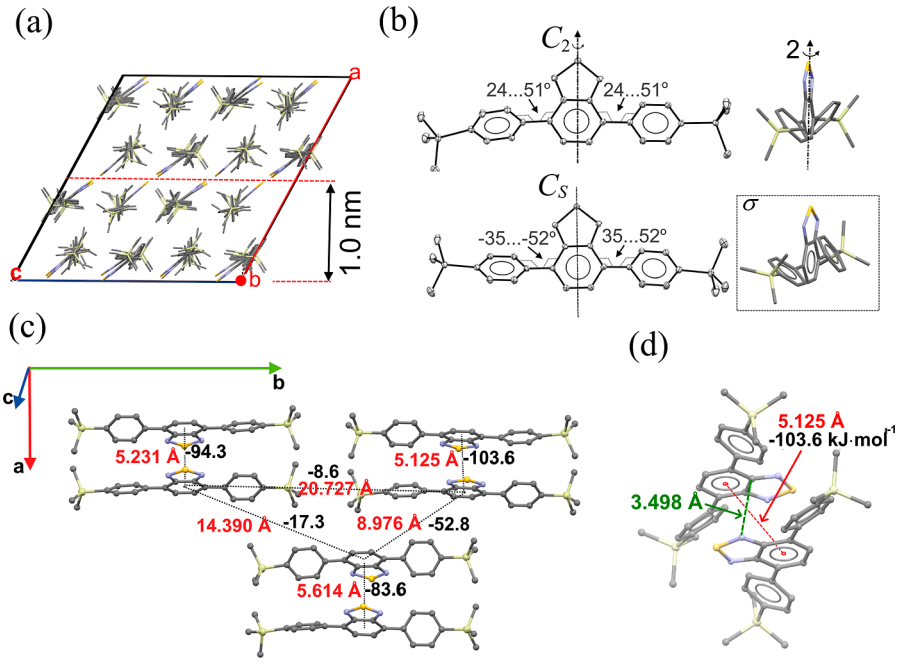

Figure 7. Crystal structure of **(TMS-P)$_2$-BTD** at 85 K: (a) unit cell projection onto the (010) plane. (b) Conformational structures of the molecules in a unit cell with the values of torsional angles in the ORTEP representation (thermal ellipsoids with a probability at the level of 50%). (c) Fragment of a unit cell indicating the potentials of pair interactions between the nearest neighbors in kJ/mol (black numbers) and the distances between the centers of the corresponding molecules. (d) Pair configuration of the closest located molecules.

is shown in Figure 7a. In the cell, the molecules are equally oriented in the [010] direction, and the **BTD** fragments are approximately parallel to the (101) plane. The linear anisotropy of crystal growth is related to the [001] direction (see Figure S5b in the Supporting Information). Accordingly, the elementary growth steps on the side face of the **(TMS-P)$_2$-BTD** crystal (Figure 5b) can correspond to 1.0 nm thick bilayers of molecules in the (100) plane orientation (Figure 7a).

The cell revealed two types of conformational structures of molecules with different higher symmetries (Figure 7b). In 75% of the molecules (24), the phenyl groups are turned in different directions relative to the **BTD** fragment, so it is possible that there is a second order rotational symmetry axis (point group C_2), while in the rest of the molecules (8) the phenyl groups are turned in one direction and their conformation can be characterized by C_S symmetry (see Figures 7b and S6 in the Supporting Information). The torsional angles between conjugated units for the molecules with C_S symmetry are about 44°, and among the molecules with C_2 symmetry, a third is about 42°, and the rest is about 31°.

The packing of **(TMS-P)$_2$-BTD** molecules in the crystal is more heterogeneous than those for **P$_2$-BTD**: some of the nearest neighbors are almost opposite to each other, while the rest are slightly shifted in the direction of the *b* axis (Figure 7c). Distances between the centers of nearest neighbors due to the spreading factor of terminal trimethylsilyl groups are higher than those for **P$_2$-BTD** molecules (compare Figures 6d and 7c). In this regard, the density of **(TMS-P)$_2$-BTD** crystals is almost 15% lower than that of **P$_2$-BTD** crystals (Table S1). Figure 7c shows a fragment of a unit cell indicating the potentials of pair interactions between the nearest molecules and the distances between their centers. The **BTD** fragments of the nearest molecules are located at a distance of about 3.5 Å and are oriented antiparallel to each other (Figure 7d). The shortest distance between the centers of molecules with the strongest interaction varies from 5.1 to 5.6 Å in the direction of the *a* axis, and their interaction potentials, respectively, from −103.6 to −84.6 kJ/mol. The weakest contacts between the nearest neighbors are carried out in the direction of the end trimethylsilyl groups (20.727 Å, −8.6 kJ/mol), and the lateral interactions with the nearest neighbors displaced along the *b* axis are 2−4 times weaker than for the molecules lying opposite to each other.

The total energy of the crystal packing calculated in the force field approximation for **P$_2$-BTD** is $\Delta H_{c,1} = -168.4$ kJ·mol^{-1}, for **(TMS-P)$_2$-BTD** − $\Delta H_{c,2} = -212.4$ kJ·mol^{-1}, which indicates on the relatively higher stability of **(TMS-P)$_2$-BTD** crystals to sublimation processes.

Absorption-Fluorescent Properties in Solutions. A detailed interpretation of the results of investigation the absorption-fluorescent properties of molecular crystals is impossible without knowledge of the electronic structure and optical characteristics of the constituent individual molecules. Therefore, the optical properties of **P$_2$-BTD** and **(TMS-P)$_2$-BTD** in dilute solutions were preliminarily studied and quantum-chemical calculations of their electronic structure were performed (see Tables S2 and S3 in the Supporting Information). The results of the investigation are presented in Figures 8 and Figure S7 in the Supporting Information as well as in Tables 2 and 3.

The absorption spectra of solutions of **P$_2$-BTD** and **(TMS-P)$_2$-BTD** molecules presented in Figure 8 consist of several absorption bands, two of which stand out significantly. The most intense is the short-wavelength band. For **P$_2$-BTD**, the position of the maximum of this band in various solvents varies from 269 to 271 nm, and the value of the extinction coefficient varies from 25,200 L·mol^{-1}·cm^{-1} to 27,300 L·mol^{-1}·cm^{-1}. The position of the maximum of the less intense long-wavelength

https://doi.org/10.1021/acsomega.3c08543
ACS Omega 2024, 9, 14932−14946

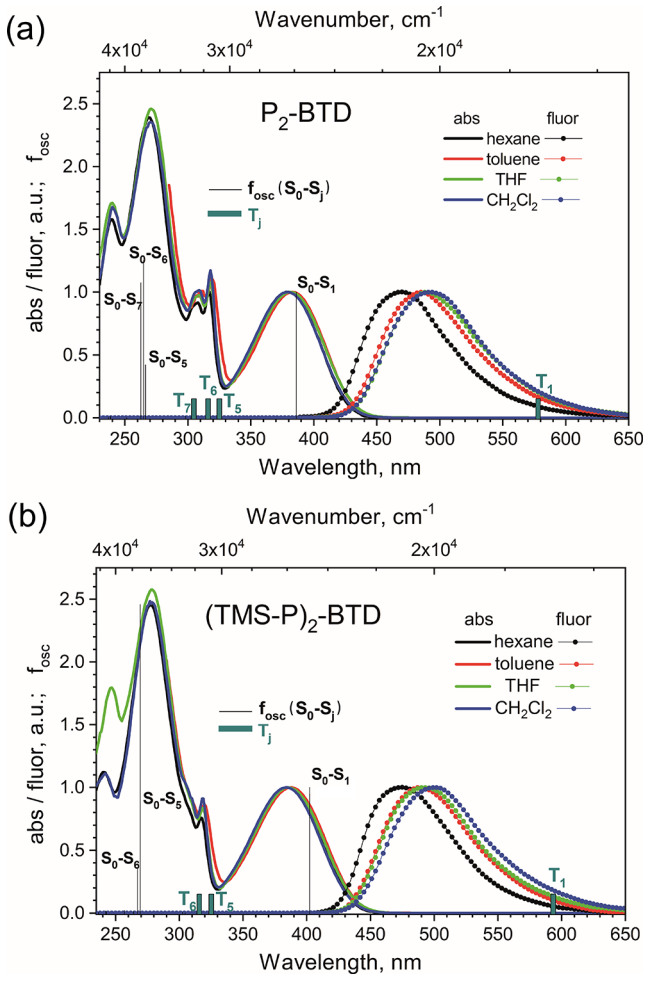

Figure 8. Absorption and fluorescence spectra of **P_2-BTD** (a) and **$(TMS\text{-}P)_2$-BTD** (b) in solutions of *n*-hexane, toluene, THF, and dichloromethane. Left axes represent the strength of the electronic transition oscillators obtained from TD DFT calculations. Dark cyan columns of the same height indicate the positions of the S_0-T_j transitions.

absorption band in the solvent series *n*-hexane−toluene−THF−dichloromethane varies from 379 to 383 nm, and the value of the extinction coefficient is from 10,600 L·mol^{-1}·cm^{-1} to 11,400 L·mol^{-1}·cm^{-1}. The experimental oscillator strength of the long-wavelength absorption band calculated from the formula $f_{osc}^{test} = n^2 \int_{\tilde{\nu}} \varepsilon(\tilde{\nu})\, d\tilde{\nu}$ in different solvents varies from 0.42 to 0.46 (Table 2). The detailed results of the quantum chemical calculation of the electronic structure of **P_2-BTD** molecule can be found in Table S2 in the Supporting Information. Figure 8 shows the position and strength of the oscillator of the most intense transitions responsible for the formation of the main absorption bands. As follows from the consideration of Figure 8a and Table S2, the long-wavelength absorption band corresponds to the $S_0 \rightarrow S_1$ (HOMO → LUMO) transition. The theoretical oscillator strength of this transition is $f_{osc1}^{calc} = 0.35$, which is 25% less than the average f_{osc1}^{test} value for four solvents (Table 2). Three transitions with close energy values are responsible for the formation of the short-wavelength band ($\Delta\tilde{\nu} \sim 300$ cm^{-1}): $S_0 \rightarrow S_2$ (HOMO → LUMO + 1) as well as two deeper electron transitions: HOMO − 4 → LUMO and HOMO − 5 → LUMO. These transitions form the intense band in the absorption spectrum of **P_2-BTD**, and the resulted excited state of **P_2-BTD** is S_1 with no evidence of the internal conversion $S_2 \rightarrow S_1$. In addition to the three main transitions, in the wavelength range from 320 to 230 nm, there are weak transitions with an oscillator strength ≤0.0042 (Figure 8a and Table S2).

The contour of the absorption spectrum of the compound **$(TMS\text{-}P)_2$-BTD** is very similar to the absorption spectrum of **P_2-BTD** (compare Figure 8a,b). The extinction coefficients and the positions of the main absorption bands are shown in Table 2; the spectral distribution of the molar extinction coefficient is shown in Figure S7 in the Supporting Information. The maxima of the **$(TMS\text{-}P)_2$-BTD** absorption bands are shifted by 270−410 cm^{-1} (long-wavelength) and 900−1200 cm^{-1} (short-wavelength) toward the long-wavelength side with respect to the absorption bands of **P_2-BTD**. The experimental oscillator strength f_{osc1}^{test}, obtained by calculating the value of the integral extinction coefficient of the long-wavelength absorption band **$(TMS\text{-}P)_2$-BTD** in different solvents, varies from 0.52 to 0.58 (Table 2). The detailed results of the quantum chemical calculation of the electronic structure of **$(TMS\text{-}P)_2$-BTD** can be found in Table S3 in the Supporting Information. The long-wavelength absorption band corresponds to the transition $S_0 \rightarrow S_1$ (HOMO → LUMO). The theoretical transition oscillator strength $f_{osc1}^{calc} = 0.40$. This is 30−40% less than the average f_{osc1}^{test} values obtained for four solvents (Table 2). Two intense transitions $S_0 \rightarrow S_2$ (HOMO → LUMO + 1) and deeper HOMO − 4 → LUMO are responsible for the formation of the short-wavelength band (Figure 8b and Table S3 in the Supporting Information). The difference between the energies

Table 2. Optical Properties of P_2-BTD and $(TMS\text{-}P)_2$-BTD in Solutions and in Polycrystalline Films

compound	solvent	$\lambda_{max\ 2}^{abs}$ nm	ε_2 M^{-1} cm^{-1}	$\lambda_{max\ 1}^{abs}$ nm	ε_1[a] M^{-1} cm^{-1}	f_{osc1}^{test}	f_{osc1}^{calc}	λ_{max}^{fluor} nm	fwhm[b] fluorescence, cm^{-1}
P_2-BTD	hexane	269	27,300	379	11,400	0.42	0.35	469	3570
	toluene			383	10,600	0.46		486	3510
	THF	271	27,100	381	11,000	0.44		490	3510
	CH_2Cl_2	270	25,200	379	10,700	0.44		492	3540
	crystal			380	4600 cm^2/g			493	2500
$(TMS\text{-}P)_2$-BTD	hexane	278	35,300	385	14,400	0.52	0.40	475	3430
	toluene			388	13,300	0.58		489	3400
	THF	278	35,800	385	13,900	0.56		492	3410
	CH_2Cl_2	277	33,800	384	13,600	0.56		500	3440
	crystal			383	5900 cm^2/g			490	2610

[a]Notes:The weight coefficient of absorption is given for a polycrystalline film $k_{abs}^{mass} = (\lg(I_0/I)/d)$, where *d* is the surface density (thickness) of the polycrystalline layer (g/cm^2). [b]fwhm, full width at half-maximum.

https://doi.org/10.1021/acsomega.3c08543
ACS Omega 2024, 9, 14932−14946

Table 3. Quantum Yield and Kinetic Characteristics of Diluted Solutions and Crystals of P_2-BTD and $(TMS\text{-}P)_2$-BTD Molecules

compound	solvent	$\varphi(\varepsilon_D,n)$	QY_{fluor} [a]	τ_{fluor} [b] (ns)	k_r (ns^{-1})	k_{nr} (ns^{-1})	k_{rBD} (ns^{-1})	Stokes shift (cm^{-1})	μ_e/μ_g
P_2-BTD	hexane	1.8×10^{-4}	0.83	5.5	0.151	0.031	0.092	5060	5.23/0.24
	toluene	–	0.93	7.8	0.119	0.009	0.094	5530	
	THF	0.4344	0.95	9.1	0.104	0.005	0.085	5840	
	CH_2Cl_2	0.4740	0.96	10.7	0.090	0.004	0.086	6060	
	crystal		0.50	5.0	0.100			3900	
$(TMS\text{-}P)_2$-BTD	hexane	–//–	0.75	5.1	0.148	0.049	0.113	4920	5.80/0.30
	toluene	–	0.89	6.8	0.131	0.016	0.117	5320	
	THF	–//–	0.96	7.9	0.122	0.005	0.109	5650	
	CH_2Cl_2	–//–	0.98	9.0	0.109	0.002	0.105	6040	
	crystal		0.85	7.7	0.110			3500	

[a]Notes: the error of QY_{fluor} determination for solutions is ±0.03. The error of QY_{fluor} determination for crystals is given in the text. [b]The error of τ_{fluor} determination for solutions is ±0.05 ns. The error of τ_{fluor} determination for crystals is given in the text.

of these transitions is 307 cm^{-1}. In addition to the main peaks, the absorption spectrum of $(TMS\text{-}P)_2$-BTD contains weak transitions with an oscillator strength ≤0.006 (Table S3).

Fluorescence spectra of solutions of P_2-BTD and $(TMS\text{-}P)_2$-BTD molecules in *n*-hexane, toluene, THF, and dichloromethane presented in Figure 8 consist of a single structureless band mirror-symmetrical to the long-wavelength absorption band. The position of the maximum of the P_2-BTD and $(TMS\text{-}P)_2$-BTD fluorescence bands shifts bathochromically with increasing the solvent polarity (Table 2). The magnitude of the Stokes shift during the transition from *n*-hexane to dichloromethane increases by 1000 cm^{-1} for P_2-BTD and 1120 cm^{-1} for $(TMS\text{-}P)_2$-BTD (Table 2).

The effect of the solvent on the absorption and fluorescence spectra of molecules (solvatofluorochromism) is considered in detail in the works of Liptay.[37,38] The theory of Liptey establishes a linear relationship between the differences and sums of absorption ($\tilde{\nu}_{abs}$) and emission ($\tilde{\nu}_{em}$) frequencies with the empirical functions of solvent polarity (f(n) and $\varphi(\varepsilon_D,n)$).[39−41] By determining the slope coefficients of these dependencies, one can obtain the values of static dipole moments of the molecule in the ground (μ_g) and excited (μ_e) states (for more details, see the SI).

The values of μ_g and μ_e given in Tables 3 and S4 in the Supporting Information indicate that the insignificant polarity of the P_2-BTD and $(TMS\text{-}P)_2$-BTD molecules in the ground state (≤0.3 D) increases sharply upon transition to the first excited state (≥5 D). It is likely that such significant change in polarity is caused by the localization of the electron density on the central BTD fragment of the molecules.

The results of the investigation of the solvent influence on the quantum yield and kinetic characteristics of the fluorescence of P_2-BTD and $(TMS\text{-}P)_2$-BTD molecules are presented in Table 3 and Figure S10 in the Supporting Information. In the solvent series of *n*-hexane−toluene−THF−dichloromethane, the fluorescence quantum yield QY_{fluor} of the molecules increases from 0.83 to 0.96 for P_2-BTD and from 0.75 to 0.98 for $(TMS\text{-}P)_2$-BTD. The fluorescence lifetime τ_{fluor} increases even more significantly: from 5.5 to 10.7 ns for P_2-BTD and from 5.1 to 9.0 ns for $(TMS\text{-}P)_2$-BTD. The reasons for the increase in QY_{fluor} and τ_{fluor} with increasing the solvent polarity become clear if we consider the dependences of the values of the radiative k_r and nonradiative k_{nr} constants corresponding to the $S_1 \rightarrow S_0$ transition on the Stokes shift (or solvent polarity). These dependencies are shown in Figure 9 (see also Table 3). The value of k_r decreases linearly with

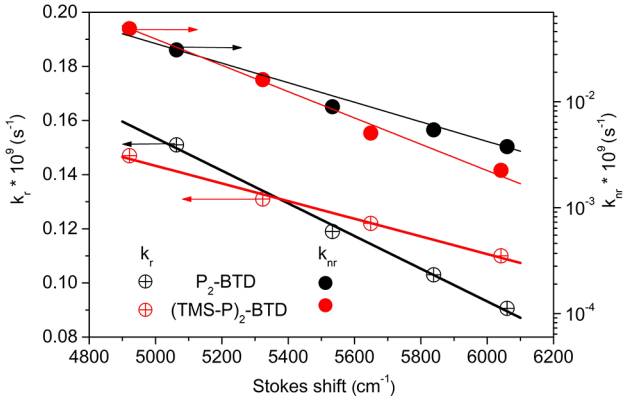

Figure 9. Dependence of the radiative k_r and nonradiative k_{nr} constants on the Stokes shift of P_2-BTD and $(TMS\text{-}P)_2$-BTD molecules in different solvents. Dots are experimental values and lines are approximations.

increasing Stokes shift, while k_{nr} decreases exponentially (the right axis in Figure 9 is exponential). A faster decrease in the value of k_{nr} than for the radiation constant ($S_1 \rightarrow T_1$ conversion) leads to an increase in the quantum yield and fluorescence lifetime of the P_2-BTD and $(TMS\text{-}P)_2$-BTD molecules with increasing solvent polarity.

The change in the k_r/k_{nr} ratio may be due to the fact that during the relaxation of the solvate shell, the value of the "energy gap" between the singlet and the corresponding triplet states of the P_2-BTD and $(TMS\text{-}P)_2$-BTD molecules changes. Figure 8, in addition to the positions and strengths of the oscillators of singlet−singlet transitions ($S_0 \rightarrow S_i$), shows the positions of the corresponding singlet−triplet transitions ($S_0 \rightarrow T_i$). According to quantum chemical calculations, with the optimized geometry of free P_2-BTD and $(TMS\text{-}P)_2$-BTD molecules (isolated from the environment), the "energy gap" between the S_1 and T_1 states is 1.06 and 0.99 eV, respectively. With such a large energy gap, the probability of $S_1 \rightarrow T_1$ conversion is very low, and the fluorescence quantum yield will be close to unity. Changes in the probability of singlet−singlet and singlet−triplet transitions can be caused by changes in the normal geometry of a dissolved molecule as a result of its interaction with solvent molecules. If, as a result of a change in the geometry of the nuclear core of a dissolved molecule, the probability of $S_1 \rightarrow S_0$ decreases or the probability of $S_1 \rightarrow T_1$ transitions increases, then the quantum yield and fluorescence lifetime decrease.

https://doi.org/10.1021/acsomega.3c08543
ACS Omega 2024, 9, 14932−14946

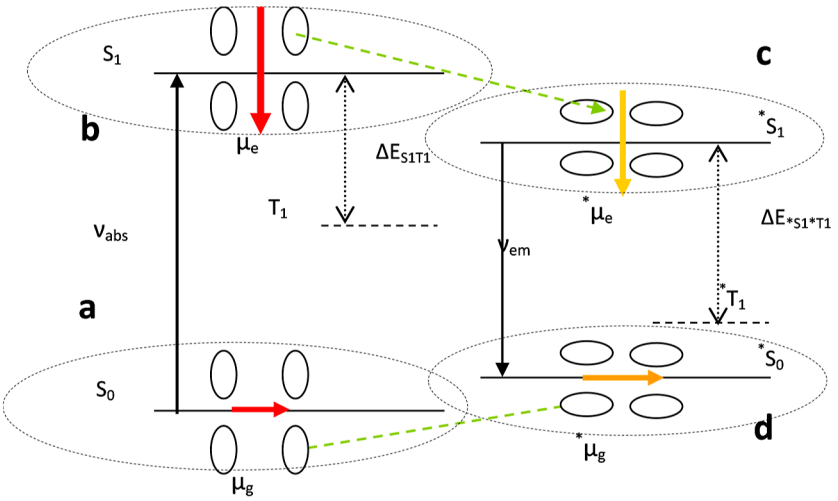

Figure 10. Change in the solvation of molecules after excitation and emission. The colored arrows indicate a probable direction of the dipole moments. The small solid ovals are solvent molecules. (**a**−**d**) Different states of the dissolved molecule.

A change in the geometry of the nuclear core of a dissolved molecule in the ground (unexcited) state should lead to changes in the wavelength (λ_{max}) and/or intensity (ε_{max}) of absorption. In the case of **P$_2$-BTD** and **(TMS-P)$_2$-BTD** molecules, this does not take place. In all four solvents, the maximum of the long−wavelength absorption band corresponds to a wavelength range of ±2 nm, and the difference between the values of the extinction coefficients is only 3−4% (Table 2). Therefore, the change in the equilibrium geometry occurs in the excited state.

This conclusion can be confirmed by comparing the values of k_r obtained in the experiment with the values of the radiation constant $k_{r,BD}$ calculated by the Birks−Dyson formula 1[42]

$$k_{r,BD} = 2.880\cdot10^{-9}\left(\frac{g_0}{g_1}\right)\left(\frac{n_{fluor}^3}{n_{abs}}\right)\frac{\int_{\tilde{\nu}}\frac{\varepsilon(\tilde{\nu})\,d\tilde{\nu}}{\tilde{\nu}}}{\int_{\tilde{\nu}}\frac{I(\tilde{\nu})\,d\tilde{\nu}}{\tilde{\nu}^3}/\int_{\tilde{\nu}}I(\tilde{\nu})\,d\tilde{\nu}} \quad (1)$$

where g_0 and g_1 are the multiplicities of the ground and excited states; $\varepsilon(\tilde{\nu})$ and $I(\tilde{\nu})$ are the spectral dependences of the molar extinction coefficient and fluorescence intensity on the wavenumber $\tilde{\nu}$, respectively; and n_{abs} and n_{fluor} are the refractive index values of the solvent corresponding to the spectral regions of the absorption and fluorescence bands of the molecule.

Calculations by formula 1 give good agreement with the experimental values of the fluorescence rate constant of those molecules whose nuclear configurations in the ground and excited states differ a little. Otherwise, there are significant discrepancies. Table 3 shows the experimental k_r and calculated $k_{r,BD}$ values of the radiation constant of the **P$_2$-BTD** and **(TMS-P)$_2$-BTD** molecules. As can be seen, the calculated values of $k_{r,BD}$ in the series of *n*-hexane, toluene, THF, and dichloromethane solvents change by no more than 7%, while the experimental values of k_r in the same series decrease by 40% for **P$_2$-BTD** and by 25% for **(TMS-P)$_2$-BTD**. Consequently, the configurations of the nuclear core of the **P$_2$-BTD** and **(TMS-P)$_2$-BTD** compounds in the S_1 state change significantly.

A visual representation of the mechanism of change in the configuration of the nuclear core of **P$_2$-BTD** and **(TMS-P)$_2$-BTD** molecules in the excited state can be obtained by considering the scheme of processes that occur after the absorption of a photon by a molecule in a solvent (Figure 10). In Figure 10, the solvating molecules are schematically represented by small ovals. The solid horizontal lines indicate the energy levels of the ground S_0 and excited S_1 singlet states of the dissolved molecule. The dashed horizontal lines denote the T_1 triplet state. The colored arrows schematically indicate the static dipole moments of the molecule in the ground μ_g and excited μ_e states. The sign (*) next to the state symbol or dipole moment indicates that they belong to a molecule with a modified geometry.

Both in the ground S_0 state and in the excited S_1 state, the dissolved molecule is solvated due to dipole−dipole or dipole-induced interactions with solvent molecules. Before the absorption of a photon ν_{abs}, the dissolved molecule and the solvent molecules are in an equilibrium state (a). After absorption of a photon, the dipole moment and polarizability of the molecule instantly (within ∼10^{-15} s) change, and the distribution of solvent molecules does not have time to change (b). In this state, the dissolved molecule and the solvent molecules are nonequilibrium solvated. Since the lifetime of the excited state S_1 is quite long (5−10 ns, see Table 3), even before the emission of a photon ν_{em}, the system relaxes into an equilibrium state with a lower energy (c). In this state, the dissolved molecule and the solvent molecules are solvated in equilibrium. In the process of relaxation to the equilibrium state (c), the mutual repulsion (van der Waals forces) of the atoms of the dissolved molecule and solvent molecules can, in some cases, lead to a change in the geometry of the dissolved molecule. It is known that the rotation energy of the C−C bond is only 0.8 kcal·mol^{-1}·rad^{-1} or 0.035 eV·rad^{-1}.[43] Therefore, changes in the geometry of the **P$_2$-BTD** and **(TMS-P)$_2$-BTD** molecules are most likely as a result of rotation along the C−C bond between the central **BTD** fragment and the side phenyl rings. As a result, the configuration of the nuclei of the dissolved molecule in the excited equilibrium state (c) will differ from the configuration of its nuclei in the ground equilibrium state (a).

The energy of electronic states and the probabilities of transitions between them are largely determined by the configuration of the core nuclei of the molecule. Consequently, the structure of electronic transitions and the strength of

https://doi.org/10.1021/acsomega.3c08543
ACS Omega 2024, 9, 14932−14946

oscillators in state (c) will differ from the structure of electronic transitions and the strength of oscillators of a dissolved molecule in state (a). After the emission of a photon ν_{em}, the dissolved molecule and solvent molecules again find themselves in a nonequilibrium state (d), from which relaxation occurs to an equilibrium state (a) with the restoration of the configuration of the dissolved molecule. It is likely that the change in the configuration of the **P_2-BTD** and **$(TMS\text{-}P)_2$-BTD** molecules in the excited state is due to a large change in the static dipole moment during the transition from the S_0 state to the S_1 state (5−5.5 D, see Table 3). Therefore, in the solvents with different polarities, the conformation of **P_2-BTD** and **$(TMS\text{-}P)_2$-BTD** molecules will vary to a different degree.

Thus, the reasons for increasing the values of the fluorescence quantum yield and the lifetime increase with increasing the solvent polarity can be summarized as follows. The transitions to the first electronic excited state of the **P_2-BTD** and **$(TMS\text{-}P)_2$-BTD** molecules are characterized by a significant change in the electron density distribution. The associated instantaneous increase in the static dipole moment changes the configuration of the forces of interaction between the solvent molecules and the fragments of the molecules investigated. In the process of solvate relaxation to a new equilibrium state, due to the fact that an insignificant energy (∼0.04 eV/rad) is required to change the torsional angle between the side phenyl rings and the central **BTD** fragment, not only the solvate shell is rearranged, but also the conformation of the molecules themselves changes. The new equilibrium distribution of the solvation shell molecules and the changed geometry of the atomic core of the **P_2-BTD** and **$(TMS\text{-}P)_2$-BTD** molecules correspond to a new mutual arrangement of the electronic states and new values of the transition probabilities between them. The calculation of the rate constants for radiative and nonradiative transitions showed that with increasing solvent polarity, probabilities of both the intersystem crossing and the fluorescent transitions decrease. The relative decrease in the probability of intersystem crossing is greater than that of the fluorescent transition. As a result, the quantum yield and fluorescence lifetime of the **P_2-BTD** and **$(TMS\text{-}P)_2$-BTD** molecules increase.

Absorption-Fluorescent Properties of the Crystals. According to the theory of excitons, the absorption of light in a molecular crystal corresponds to the transition to the energy level of an aggregate of molecules and cannot be localized. The excited state (exciton) instantly (within $\sim10^{-13}$ to 10^{-12} s) covers several hundred or even thousands of molecules. The probability of exciton disappearance in a crystal is equal to the sum of the probabilities of intrinsic fluorescence, quenching on defects in the crystal lattice or on impurity molecules. Fluorescence occurs as a result of exciton capture by fluorescent molecules, the lower excited energy level of which is located below the rest—the centers of fluorescence.[44−46]

The results of absorption-fluorescence measurements and the values of the fluorescence lifetime of crystals are presented in Figure 11, Table 3 and in Figures S9 and S11 in the Supporting Information. Measurements of the absorption and fluorescence spectra of crystals based on **P_2-BTD** and **$(TMS\text{-}P)_2$-BTD** molecules were performed for thin, tightly pressed polycrystalline layers with surface densities of d_1 = 0.2 mg·cm^{-2} and d_2 = 4 mg·cm^{-2} (thickness, 2 and 40 μm, respectively, at an average backfill density of ∼1.0 g·cm^{-3}). In the d_2 layer, the exciting light is absorbed almost completely, which is important for reliable determination of the fluorescence quantum yield; however, the fluorescence spectrum of the crystal is strongly reabsorbed, and only the long-wavelength edge can be observed in the absorption spectrum (Figures 11 and S9). In the d_1 layer, on the contrary, it is possible to accurately measure the shape of the absorption and fluorescence spectra, but it is impossible to determine the quantum yield of fluorescence. Therefore, the fluorescence intensity of the polycrystalline layer d_2 was first measured. To account for reabsorption, the short-wave edge of the fluorescence spectrum was reconstructed using the spectral distribution of the long-wave edge of the absorption spectrum. Then, the contour of the fluorescence spectrum of layer d_1 was measured and compared with the reconstructed fluorescence spectrum. This approach makes it possible to fairly accurately take into account the losses of fluorescence due to self-absorption in the crystal and calculate the "internal" fluorescence quantum yield corrected for reabsorption (Table 3).

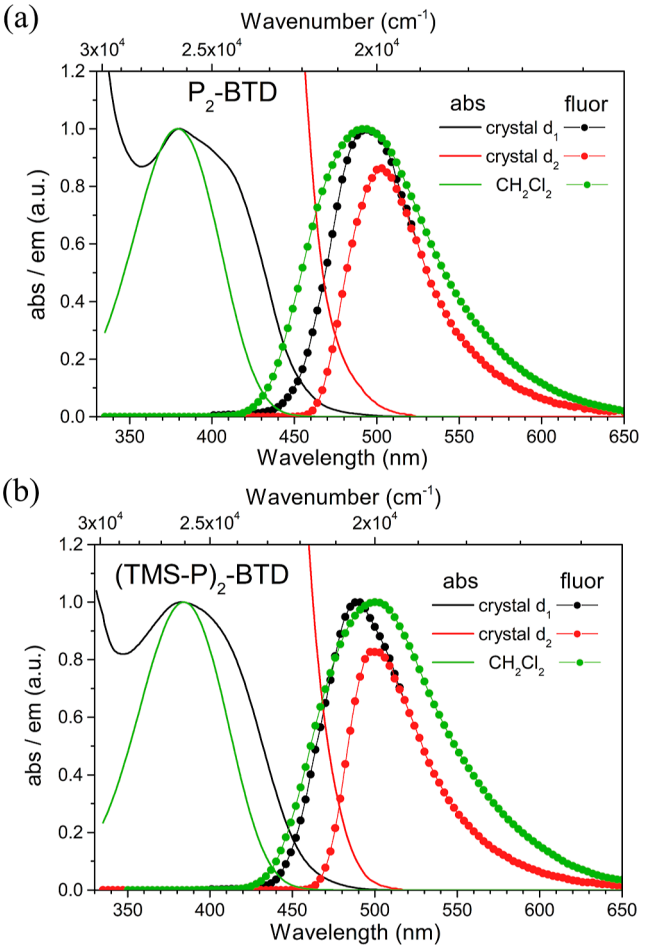

Figure 11. Absorption and fluorescence spectra of the crystals of **P_2-BTD** (a) and **$(TMS\text{-}P)_2$-BTD** (b) molecules.

The position of the maximum of the long-wavelength band in the absorption spectrum of a thin layer of microcrystals (d_1) of **P_2-BTD** corresponds to the position of the maximum of the long-wavelength band in the absorption spectrum of **P_2-BTD** in CH_2Cl_2 (379 and 380 nm, Figure 11a, Table 3). The contour of the absorption band of microcrystals in the d_1 layer has a larger width and a more complex shape than the contour

https://doi.org/10.1021/acsomega.3c08543
ACS Omega 2024, 9, 14932−14946

of the absorption band of **P_2-BTD** in CH_2Cl_2. The broadening of the absorption spectrum of the crystal compared to the absorption spectrum in CH_2Cl_2 can be explained by the spread in the values of the intermolecular interaction energy between neighboring molecules (see Figure 6d). An additional broadening of the absorption spectrum can be caused by the exciton splitting of the excited states of the molecules.[44−46]

The maximum of the fluorescence spectrum of microcrystals in the d_1 layer coincides with the maximum of the fluorescence spectrum of **P_2-BTD** in CH_2Cl_2 (493 and 492 nm, Table 3). The width of the fluorescence spectral contour of the crystal is smaller than the width of the fluorescence spectrum in CH_2Cl_2 (see Figure 11a, Table 3). The frequency of the 0−0 transition in the crystal is $\nu_{0-0}{}^{cryst}$ = 22,200 cm^{-1} and it is shifted by 900 cm^{-1} to lower frequencies with respect to the frequency of the 0−0 transition in CH_2Cl_2 $\nu_{0-0}{}^{solv}$ = 23,100 cm^{-1} (see Table S5).

Knowing the frequency ν_{0-0}^{Cryst}, it is possible, using the mathematical notation of the mirror symmetry rule for the absorption and fluorescence spectra ($\nu_{max}^{abs} + \nu_{max}^{fluor} = 2\nu_{0-0}$), to determine the frequency of absorption of light by the fluorescence center in the crystal ($\lambda_{fluor.center}^{abs}$), as well as the Stokes shift. In a **P_2-BTD** crystal, $\lambda_{fluor.center}^{abs}$ = 413 nm (24,200 cm^{-1}, see Table S5). There is an inflection on the absorption spectrum of a thin layer of microcrystals **P_2-BTD** at this wavelength (Figure 11a). It can be assumed that this inflection refers to the absorption of light by the fluorescence centers of the **P_2-BTD** crystal. The Stokes shift for the **P_2-BTD** crystal is 3880 cm^{-1}. This value is significantly less than the Stokes shift value for a solution of **P_2-BTD** in CH_2Cl_2 (6060 cm^{-1}, Table 3). As shown above, the value of the Stokes shift of the **P_2-BTD** compound in *n*-hexane−toluene−THF−dichloromethane solvent series increases with increasing their polarity (Table 3). This is due to the rearrangement of the solvate shell of the dissolved molecule. There is no rearrangement of the near surrounding in the crystal; therefore, there is no increase in the Stokes shift, and the width of the fluorescence spectrum of the crystal is smaller compared to that in solution.[47]

The fluorescence quantum yield QY_{fluor} of a crystal based on **P_2-BTD** is almost two times lower than those in CH_2Cl_2 (0.50 ± 0.05 versus 0.96 ± 0.03), as is the fluorescence decay time τ_{fluor} (5.0 ± 0.4 ns and 10.70 ± 0.05 ns, respectively, see Table 3). As a result, the fluorescence rate constant for the **P_2-BTD** crystal and for the solution in CH_2Cl_2 turns out to be the same within the measurement error: k_r = 0.100 ns^{-1} in the crystal and k_r = 0.090 ns^{-1} in the solution. Therefore, the decrease in the fluorescence quantum yield of the **P_2-BTD** crystal compared to the solution in CH_2Cl_2 is due to nonradiative energy losses in the crystal and not due to a decrease in the rate of radiative transition of the fluorescence center.

For the **$(TMS\text{-}P)_2$-BTD** molecule, the contour of the absorption band of the microcrystalline layer is very similar to the absorption contour of **P_2-BTD** (Figure 11b). As in the case of **P_2-BTD**, the position of the maximum of the long-wavelength absorption band of the microcrystals corresponds to the position of the maximum of the long-wavelength absorption band of the solution (384 and 383 nm, Table 3). Compared to the position of the maximum of the fluorescence spectrum of **$(TMS\text{-}P)_2$-BTD** in CH_2Cl_2 (500 nm), the maximum of the fluorescence spectrum of the crystal is shifted to the short-wavelength region (490 nm). As with **P_2-BTD**, the fluorescence bandwidth of the **$(TMS\text{-}P)_2$-BTD** crystal is smaller than the fluorescence spectrum width in CH_2Cl_2 (Table 3, Figure 11b). The frequency of the 0−0 transition in the crystal $\nu_{0-0}{}^{Cryst}$ = 22,150 cm^{-1} is shifted by 650 cm^{-1} to lower frequencies in relation to the frequency of the 0−0 transition in CH_2Cl_2 $\nu_{0-0}{}^{Solv}$ = 22,800 cm^{-1} (see Table S5). The position of the absorption maximum of the fluorescence center corresponds to a wavelength of 418 nm (23,900 cm^{-1}, see Table S5). The Stokes shift for the fluorescent center is 3500 cm^{-1} (Table 3). As in the case of **P_2-BTD**, its value is significantly less than that for a solution of **$(TMS\text{-}P)_2$-BTD** in CH_2Cl_2 (6060 cm^{-1}, Table 3).

The fluorescence quantum yield of the QY_{fluor} crystal **$(TMS\text{-}P)_2$-BTD** 0.85 ± 0.05 is slightly lower than in CH_2Cl_2 (0.98 ± 0.03), as is the fluorescence lifetime (7.7 ± 0.4 and 9.00 ± 0.05 ns, respectively). The fluorescence rate constant of the **$(TMS\text{-}P)_2$-BTD** crystal has the same value as the fluorescence rate constant in CH_2Cl_2 solution: k_r = 0.110 ns^{-1} in the crystal and k_r = 0.109 ns^{-1} in CH_2Cl_2. Consequently, as in the case of **P_2-BTD**, the slightly lower quantum yield is due to nonradiative energy losses of the exciting radiation in the crystal.

It follows from a comparison of the absorption-fluorescence properties of crystals and solutions that the absorption spectra of crystals are due to transitions between the π-electron states of the **P_2-BTD** and **$(TMS\text{-}P)_2$-BTD** compounds. The fluorescence centers in crystals are molecules whose conformation corresponds to the conformation of the **P_2-BTD** and **$(TMS\text{-}P)_2$-BTD** molecules in CH_2Cl_2. The fluorescence of these molecules is due predominantly to the capture of an exciton rather than to the direct absorption of a photon of the exciting radiation. Therefore, the fluorescence quantum yield of a crystal is determined not only by the values of the radiative k_r and nonradiative k_{nr} constants of the fluorescence center but also by the efficiency of energy transfer by excitons to the fluorescence center. In this case, the fluorescence quantum yield is significantly affected by the probability of nonradiative deactivation of excitons at defects (quenching centers) of the crystal.

Under conditions of constant and continuous excitation, the following expression (2) can be written for the fluorescence quantum yield of the crystal QY_{fluotr}^{Cryst}

$$QY_{fluor}^{Cryst} = \frac{k_{EX}^{F}[F][Ex]}{k_{EX}^{F}[F][Ex] + k_{EX}^{T}[T][Ex]} QY_{fluor}^{F0} \text{ or}$$

$$\frac{QY_{fluor}^{F0}}{QY_{fluor}^{Cryst}} = \frac{\tau_{fluor}^{F0}}{\tau_{fluor}^{Cryst}} = 1 + \frac{k_{EX}^{T}[T]}{k_{EX}^{F}[F]} = 1 + K_F^T\frac{[T]}{[F]} \quad (2)$$

where QY_{fluor}^{F0} is the quantum yield of the fluorescence center of the crystal or molecule of the prototype of the fluorescence center; k_{EX}^{F} and k_{EX}^{T} are the rate constants of excitation of fluorescent centers and nonradiative deactivation (quenching) of excitons, respectively, $L{\cdot}mol^{-1}{\cdot}s^{-1}$; $[E_x]$ is the stationary concentration of singlet excitons, $mol{\cdot}L^{-1}$; and [F] and [T] are the concentration of fluorescence centers and exciton quenching (deactivation) centers, respectively, $mol{\cdot}L^{-1}$.

By measuring the values of $QY_{fluor}{}^{F0}$ and $QY_{fluor}{}^{Cryst}$, one can estimate the ratio of the rates of nonradiative $k_{EX}{}^{T}[T]$ and radiative QY_{fluor}^{Cryst} deactivation of the excitation energy or the concentrations of exciton quenching centers [T] and fluorescence centers [F] in the crystal. If we accept the parameters of the fluorescence centers as corresponding to the parameters of the **P_2-BTD** and **$(TMS\text{-}P)_2$-BTD** molecules in CH_2Cl_2, then we obtain $K_F^T\frac{[T]}{[F]}$ = 0.92 for a crystal based on **P_2-**

https://doi.org/10.1021/acsomega.3c08543
ACS Omega 2024, 9, 14932−14946

BTD; $K_F^T\frac{[T]}{[F]}$ = 0.15 for a crystal based on **(TMS-P)$_2$-BTD**. Such a significant difference is due to the different crystal structures of the **P$_2$-BTD** and **(TMS-P)$_2$-BTD** compounds (see Table S2). In the unit cell of a crystal based on **P$_2$-BTD**, the torsional angles between the phenyl groups and the central **BTD** fragment average 40 ± 4°, the spread is insignificant (Figure 6b). The packing of molecules is more ordered than in the unit cell of a crystal based on **(TMS-P)$_2$-BTD**. In contrast, in the **(TMS-P)$_2$-BTD**-based crystal, the values of the torsional angles between the phenyl groups and the central **BTD** fragment range from 26 to 52° (see Figures 7b and S6 in the Supporting Information).

Using DFT calculations of the electronic structure of **P$_2$-BTD** and **(TMS-P)$_2$-BTD** molecules, we calculated the dependence of the energy and strength of the first electron transition oscillator on the value of the torsional angle between the phenyl groups and the central **BTD**-fragment. The results of the calculation can be found in Table S6 in the Supporting Information. It follows from the data obtained that the lowest value of the energy of the first electron transition corresponds to the conformations of molecules with torsional angles of about 25°. In the unit cell of the **(TMS-P)$_2$-BTD**-based crystal, there are a significant number of molecules with the angle values close to 25°. Obviously, it is these molecules that are the centers of fluorescence. As the calculations above have shown, the ratio between quenching centers and fluorescence centers in the **(TMS-P)$_2$-BTD** crystal is ∼1/6.5. This explains the high fluorescence quantum yield of these crystals.

In the **P$_2$-BTD** crystal, the molecules with a torsional angle of about 40° between the phenyl groups and the central **BTD** fragment are dominated. Probably, there are very few molecules with a conformation corresponding to the torsional angles of 25−30° in this crystal, which does not allow us to observe them by X-ray diffraction analysis.

Thus, in the unit cell of the **(TMS-P)$_2$-BTD** crystal, the concentration of fluorescent centers is high, while in the **P$_2$-BTD** crystal, their concentration is low. As a result, the fluorescence quantum yield decreases in the latter.

CONCLUSIONS

Thus, investigation of solubility and crystallization of 4,7-diphenyl-2,1,3-benzothiadiazole **P$_2$-BTD** and its trimethylsilyl derivative **(TMS-P)$_2$-BTD** in *n*-hexane solutions allowed us to obtain the samples of single crystals of these molecules on a scale of 1 cm. It was found that both substances crystallize predominantly with 1D anisotropic growth in the form of needles and rods; however, the formation and growth of convex (bulk) crystals is less common for **(TMS-P)$_2$-BTD**. Thermoanalytical studies have shown that both **P$_2$-BTD** and **(TMS-P)$_2$-BTD** are stable compounds with melting points of 407 and 425 K, respectively, and exhibit a low level of substance loss through evaporation in the solid and liquid phases in a wide range around the melting point, which is favorable for obtaining bulk crystals of these compounds using melt techniques. By the method of single-crystal X-ray diffraction at 85 and 293 K, the crystal structure in a triclinic system with a sp. gr. $P\bar{1}$ (Z = 4) was refined for **P$_2$-BTD**, while the structure of **(TMS-P)$_2$-BTD** crystals was solved at 85 K in a monoclinic system with a sp. gr. $P2_1/c$ (Z = 32). The **(TMS-P)$_2$-BTD** crystals have a looser crystal packing with a density nearly 15% lower than that of **P$_2$-BTD** crystals. In the **P$_2$-BTD** crystals, a layered structure was observed with the presence of the most closely packed monomolecular layers in the (001) plane orientation, while for **(TMS-P)$_2$-BTD** crystals, a more inhomogeneous picture of the local environment of the nearest molecules takes place. In the unit cell of the **P$_2$-BTD** crystal is seen a single-type conformational structure of the molecules with torsional angles of |40 ± 4| between the phenyl groups and the central **BTD** fragment (a point group of molecular symmetry is C_S). However, in the **(TMS-P)$_2$-BTD** crystal, two types of conformers with the molecular symmetry close to C_2 (75%) and C_S (25%) with a wider spread of the values of the above torsional angles within 24−52° was found. These features of the crystal structure create a good background for a detailed analysis of the structure-fluorescent properties' relationship through a comparative analysis.

By studying the effect of different solvents on the optical characteristics of **P$_2$-BTD** and **(TMS-P)$_2$-BTD** molecules, it was found that the values of the fluorescence quantum yield and the lifetime increase with increasing the solvent polarity. We proposed that the reason for this effect is the change in the radiation and nonradiation constants and their ratio when going from nonpolar *n*-hexane to the polar dichloromethane solvent, which was confirmed by calculations of the first electronic transition oscillator strength and energy dependence on the torsion angle between the phenyl groups and the central BTD fragment.

The study of the absorption-fluorescent properties of **P$_2$-BTD** and **(TMS-P)$_2$-BTD** crystals revealed that absorption spectra of the crystals are formed by transitions between the π-electron states, while the fluorescence centers in pure undoped crystals are the molecules whose conformation is similar to the conformation of **P$_2$-BTD** and **(TMS-P)$_2$-BTD** molecules in CH_2Cl_2. The difference in the values of the fluorescence quantum yield and the lifetime of the **P$_2$-BTD** and **(TMS-P)$_2$-BTD** crystals is due to distinction in the crystal structure and conformational composition of the molecules in the crystals. A decrease in the quantum yield of the crystal as compared to the quantum yield of the molecule, which is the center of fluorescence, is due to the ratio between the concentrations of exciton quenching and fluorescence centers. In the **P$_2$-BTD** crystals, this ratio is close to unity. As a result, the quantum yield of the crystal is almost two times lower than the quantum yield of the **P$_2$-BTD** molecule in solution. It is possible to increase the quantum yield of the crystal by introducing into it a dosed amount of impurity close in the structure to the main molecule of the crystal, which acts as a fluorescence center. In the **(TMS-P)$_2$-BTD** crystals, the concentration of the molecules with the parameters of the fluorescence center is high and exceeds the concentration of quenching centers by a factor of 6.5. As a result, the fluorescence quantum yield of the crystals differs insignificantly from the quantum yield of **(TMS-P)$_2$-BTD** molecules in solution. As a result, the fluorescence quantum yield of **(TMS-P)$_2$-BTD** crystals exceeds those for **P$_2$-BTD** crystals (85 vs 50%), which makes the former a prospective material for optoelectronic applications.

ASSOCIATED CONTENT

Supporting Information

The Supporting Information is available free of charge at https://pubs.acs.org/doi/10.1021/acsomega.3c08543.

Crystallographic data of P2-BTD-85K (CIF)

Crystallographic data of P2-BTD-293K (CIF)

Crystallographic data of (TMS-P)2-BTD-85K (CIF)

https://doi.org/10.1021/acsomega.3c08543
ACS Omega 2024, 9, 14932−14946

Experimental details concerning ^{1}H, ^{13}C and ^{29}Si NMR spectra of **(TMS-P)$_2$-BTD**; examples of DSC curves in the first and second heating cycles; examples of crystal samples; crystal structure data; and absorption-fluorescent properties of solutions and crystals (PDF)

AUTHOR INFORMATION

Corresponding Authors

Valery A. Postnikov − *Kurchatov Complex of Crystallography and Photonics of the National Research Centre "Kurchatov Institute", Moscow, 119333, Russian Federation; Enikolopov Institute of Synthetic Polymer Materials of Russian Academy of Sciences, Moscow 117393, Russian Federation;* orcid.org/0000-0002-8633-2369; Email: postva@yandex.ru

Sergey A. Ponomarenko − *Enikolopov Institute of Synthetic Polymer Materials of Russian Academy of Sciences, Moscow 117393, Russian Federation;* orcid.org/0000-0003-0930-7722; Email: ponomarenko@ispm.ru

Authors

Nataliya I. Sorokina − *Kurchatov Complex of Crystallography and Photonics of the National Research Centre "Kurchatov Institute", Moscow, 119333, Russian Federation;* orcid.org/0000-0002-9105-9272

Artem A. Kulishov − *Kurchatov Complex of Crystallography and Photonics of the National Research Centre "Kurchatov Institute", Moscow, 119333, Russian Federation; Enikolopov Institute of Synthetic Polymer Materials of Russian Academy of Sciences, Moscow 117393, Russian Federation*

Georgy A. Yurasik − *Kurchatov Complex of Crystallography and Photonics of the National Research Centre "Kurchatov Institute", Moscow, 119333, Russian Federation; Enikolopov Institute of Synthetic Polymer Materials of Russian Academy of Sciences, Moscow 117393, Russian Federation*

Timofei A. Sorokin − *Kurchatov Complex of Crystallography and Photonics of the National Research Centre "Kurchatov Institute", Moscow, 119333, Russian Federation; Enikolopov Institute of Synthetic Polymer Materials of Russian Academy of Sciences, Moscow 117393, Russian Federation;* orcid.org/0000-0003-0570-742X

Maria S. Lyasnikova − *Kurchatov Complex of Crystallography and Photonics of the National Research Centre "Kurchatov Institute", Moscow, 119333, Russian Federation*

Oleg V. Borshchev − *Enikolopov Institute of Synthetic Polymer Materials of Russian Academy of Sciences, Moscow 117393, Russian Federation;* orcid.org/0000-0003-3134-9857

Maxim S. Skorotetcky − *Enikolopov Institute of Synthetic Polymer Materials of Russian Academy of Sciences, Moscow 117393, Russian Federation;* orcid.org/0000-0002-0413-0502

Sergey A. Pisarev − *Department of Chemistry, Lomonosov Moscow State University, Moscow 119991, Russian Federation; Enikolopov Institute of Synthetic Polymer Materials of Russian Academy of Sciences, Moscow 117393, Russian Federation;* orcid.org/0000-0003-0262-4397

Evgeniya A. Svidchenko − *Enikolopov Institute of Synthetic Polymer Materials of Russian Academy of Sciences, Moscow 117393, Russian Federation*

Nikolay M. Surin − *Enikolopov Institute of Synthetic Polymer Materials of Russian Academy of Sciences, Moscow 117393, Russian Federation;* orcid.org/0000-0003-1185-5699

Complete contact information is available at: https://pubs.acs.org/10.1021/acsomega.3c08543

Author Contributions

The manuscript was written through contributions of all authors. All authors have given approval to the final version of the manuscript.

Notes

The authors declare no competing financial interest.

ACKNOWLEDGMENTS

This work was carried out with financial support by the Russian Science Foundation grant no. 22-13-00255 using the scientific equipment of the Shared Research Center "Structural Diagnostics of Materials" of the NRC "Kurchatov Institute" and the Shared Research Center "Polymer Research Center" of the ISPM RAS supported by the Russian Ministry of Science and Higher Education (topic FFSM-2024-0003).

ABBREVIATIONS

BTD, benzothiadiazole fragment; P$_2$-BTD, 4,7-diphenyl-2,1,3-benzothiadiazole; (TMS-P)$_2$-BTD, 4,7-bis(4-trimethylsilyl)-phenyl)benzothiadiazole; THF, tetrahydrofuran; POPOP, 1,4-bis(5-phenyloxazol-2-yl) benzene; GPC, gel permeation chromatography; PTFE, polytetrafluoroethylene; DSC, differential scanning calorimetry; TGA, thermogravimetric analysis; AFM, atomic force microscopy; SCXRD, single crystal X-ray diffraction; TD DFT, time-dependent density functional theory; QY, quantum yield

REFERENCES

(1) Aldakov, D.; Palacios, M. A.; Anzenbacher, P. Benzothiadiazoles and Dipyrrolyl Quinoxalines with Extended Conjugated Chromophores-Fluorophores and Anion Sensors. *Chem. Mater.* **2005**, *17* (21), 5238−5241.

(2) Zhang, X.; Yamaguchi, R.; Moriyama, K.; Kadowaki, M.; Kobayashi, T.; Ishi-i, T.; Thiemann, T.; Mataka, S. Highly Dichroic Benzo-2,1,3-Thiadiazole Dyes Containing Five Linearly π-Conjugated Aromatic Residues, with Fluorescent Emission Ranging from Green to Red, in a Liquid Crystal Guest-Host System. *J. Mater. Chem.* **2006**, *16* (8), 736−740.

(3) Xu, Y.; Ren, L.; Dang, D.; Zhi, Y.; Wang, X.; Meng, L. A Strategy of "Self-Isolated Enhanced Emission" to Achieve Highly Emissive Dual-State Emission for Organic Luminescent Materials. *Chem.—Eur. J.* **2018**, *24* (41), 10383−10389.

(4) Skorotetcky, M. S.; Krivtsova, E. D.; Borshchev, O. V.; Surin, N. M.; Svidchenko, E. A.; Fedorov, Y. V.; Pisarev, S. A.; Ponomarenko, S. A. Influence of the Structure of Electron-Donating Aromatic Units in Organosilicon Luminophores Based on 2,1,3-Benzothiadiazole Electron-Withdrawing Core on Their Absorption-Luminescent Properties. *Dyes Pigm.* **2018**, *155*, 284−291.

(5) Liao, R.; Gu, S.; Wang, X.; Zhang, X.; Xie, X.; Sun, H.; Huang, W. Approaching an Adjustable Organic Thermochromic Luminophore Library: Via the Synergistic Effects between Structure-Related Molecular Dynamics and Aggregation-Related Luminescence. *J. Mater. Chem. C* **2020**, *8* (25), 8430−8439.

(6) Boehme, S. C.; Tchamba Yimga, N.; Frick, A.; Gunst, S.; Untenecker, H.; Kennis, J. T. M.; van Stokkum, I. H. M.; Kirsch, P.; von Hauff, E. Correlating Ultrafast Dynamics, Liquid Crystalline Phases, and Ambipolar Transport in Fluorinated Benzothiadiazole Dyes. *Adv. Electron. Mater.* **2021**, *7* (8), 2100186.

(7) Squeo, B. M.; Bertini, F.; Scavia, G.; Uslenghi, M.; Fois, E. S.; Pasini, M.; Botta, C. Polarized Emission and Mechanofluorochromism of Benzothiadiazole Based Chromophores Oriented by Rubbing. *Dyes Pigm.* **2022**, *204* (March), 110473.

(8) Postnikov, V. A.; Sorokina, N. I.; Kulishov, A. A.; Lyasnikova, M. S.; Grebenev, V. V.; Voloshin, A. E.; Borshchev, O. V.; Skorotetcky, M. S.; Surin, N. M.; Svidchenko, E. A.; Ponomarenko, S. A. Highly Luminescent Crystals of a Novel Linear π-Conjugated Thio-phene-Phenyl-ene Co-Oligomer with a Benzo-thia-diazole Fragment. *Acta Crystallogr., Sect. B: Struct. Sci., Cryst. Eng. Mater.* **2019**, *75*, 1076−1085.
(9) Postnikov, V. A.; Sorokina, N. I.; Kulishov, A. A.; Lyasnikova, M. S.; Sorokin, T. A.; Freidzon, A. Y.; Stepko, A. S.; Borshchev, O. V.; Skorotetsky, M. S.; Surin, N. M.; Svidchenko, E. A.; Ponomarenko, S. A. A New Linear Phenyloxazole-Benzothiadiazole Luminophore: Crystal Growth, Structure and Fluorescence Properties. *Acta Crystallogr., Sect. B: Struct. Sci., Cryst. Eng. Mater.* **2022**, *78* (2), 261−269.
(10) Echeverri, M.; Martín, I.; Concellón, A.; Ruiz, C.; Anselmo, M. S.; Gutiérrez-Puebla, E.; Serrano, J. L.; Gómez-Lor, B. Fluorescent and Electroactive Monoalkyl BTD-Based Liquid Crystals with Tunable Self-Assembling and Electronic Properties. *ACS Omega* **2018**, *3* (9), 11857−11864.
(11) Taylor, D.; Malcomson, T.; Zhakeyev, A.; Cheng, S.; Rosair, G. M.; Marques-Hueso, J.; Xu, Z.; Paterson, M. J.; Dalgarno, S. J.; Vilela, F. 4,7-Diarylbenzo[c] [1,2,5]Thiadiazoles as Fluorophores and Visible Light Organophotocatalysts. *Org. Chem. Front.* **2022**, *9*, 5473−5484.
(12) Raimundo, J. M.; Blanchard, P.; Brisset, H.; Akoudad, S.; Roncali, J. Proquinoid Acceptors as Building Blocks for the Design of Efficient π- Conjugated Fluorophores with High Electron Affinity. *Chem. Commun.* **2000**, No. 11, 939−940.
(13) Ishi-I, T.; Tanaka, H.; Youfu, R.; Aizawa, N.; Yasuda, T.; KatoMatsumoto, S. T.; Matsumoto, T. Mechanochromic Fluorescence Based on a Combination of Acceptor and Bulky Donor Moieties: Tuning Emission Color and Regulating Emission Change Direction. *New J. Chem.* **2019**, *43* (13), 4998−5010.
(14) Kato, S. I.; Matsumoto, T.; Ishi-I, T.; Thiemann, T.; Shigeiwa, M.; Gorohmaru, H.; Maeda, S.; Yamashita, Y.; Mataka, S. Strongly Red-Fluorescent Novel Donor-π-Bridge-Acceptor-π-Bridge-Donor (D-π-A-π-D) Type 2,1,3-Benzothiadiazoles with Enhanced Two-Photon Absorption Cross-Sections. *Chem. Commun.* **2004**, No. 20, 2342−2343.
(15) Kato, S. I.; Matsumoto, T.; Shigeiwa, M.; Gorohmaru, H.; Maeda, S.; Ishi-i, T.; Mataka, S. Novel 2,1,3-Benzothiadiazole-Based Red-Fluorescent Dyes with Enhanced Two-Photon Absorption Cross-Sections. *Chem.—Eur. J.* **2006**, *12* (8), 2303−2317.
(16) Postnikov, V. A.; Odarchenko, Y. I.; Iovlev, A. V.; Bruevich, V. V.; Pereverzev, A. Y.; Kudryashova, L. G.; Sobornov, V. V.; Vidal, L.; Chernyshov, D.; Luponosov, Y. N.; Borshchev, O. V.; Surin, N. M.; Ponomarenko, S. A.; Ivanov, D. A.; Paraschuk, D. Y. Molecularly Smooth Single-Crystalline Films of Thiophene-Phenylene Co-Oligomers Grown at the Gas-Liquid Interface. *Cryst. Growth Des.* **2014**, *14* (4), 1726−1737.
(17) Postnikov, V. A.; Sorokina, N. I.; Alekseeva, O. A.; Kulishov, A. A.; Sokolnikov, R. I.; Lyasnikova, M. S.; Grebenev, V. V.; Borshchev, O. V.; Skorotecky, M. S.; Surin, N. M.; Svidchenko, E. A.; Ponomarenko, S. A.; Voloshin, A. E. Growth from Solutions, Structure, and Photoluminescence of Single-Crystal Plates of p-Terphenyl and Its Trimethylsilyl Derivative. *Crystallogr. Rep.* **2018**, *63* (5), 819−831.
(18) Postnikov, V. A.; Lyasnikova, M. S.; Kulishov, A. A.; Grebenev, V. V.; Borshchev, O. V. Solubility and Crystal Growth of P-Quaterphenyl and Its Derivative with Trimethylsilyl Terminal Substituents. *Russ. J. Phys. Chem. A* **2019**, *93* (9), 1741−1746.
(19) Mo, D.; Chen, Z.; Han, L.; Lai, H.; Chao, P.; Zhang, Q.; Tian, L.; He, F. Highly Stable and Bright Fluorescent Chlorinated Polymer Dots for Cellular Imaging. *New J. Chem.* **2019**, *43* (6), 2540−2549.
(20) Hanss, D.; Wenger, O. S. Conformational Effects on Long-Range Electron Transfer: Comparison of Oligo-p-Phenylene and Oligo-p-Xylene Bridges. *Eur. J. Inorg. Chem.* **2009**, *2009* (25), 3778−3790.
(21) Postnikov, V. A.; Sorokina, N. I.; Kulishov, A. A.; Yurasik, G. A.; Lyasnikova, M. S.; Sorokin, T. A.; Skorotetsky, M. S.; Borshchev, O. V. Growth, Structure, and Phase Behavior of Di- Tert -Butyl- Para -Terphenyl Crystals. *Crystallogr. Rep.* **2023**, *68* (1), 137−146.
(22) *Gwiddion*, version 2.59; Software for scanning probe microscopy data visualization and analysis; Czech Metrology Institute: Jihlava, Czech, 2020.
(23) *CrysAlisPro*, version 171.41_64.88a; Software for single crystal X-ray diffraction; Rigaku Corporation: Tokyo, Japan, 2018.
(24) Petříček, V.; Dušek, M.; Palatinus, L. Crystallographic Computing System JANA2006: General Features. *Z. Kristallogr.* **2014**, *229* (5), 345−342.
(25) Palatinus, L. Ab Initio Determination of Incommensurately Modulated Structures by Charge Flipping in Superspace. *Acta Crystallogr., Sect. A: Found. Crystallogr.* **2004**, *60* (6), 604−610.
(26) *Mercury*, version 2022.2.0; Software for Crystal Structure Visualization, Exploration and Analysis; The Cambridge Crystallographic Data Centre: Cambridge, UK, 2022.
(27) Gavezzotti, A. Are Crystal Structures Predictable? *Acc. Chem. Res.* **1994**, *27* (10), 309−314.
(28) Crosby, G. A.; Demas, J. N. Measurement of photoluminescence quantum yields. Review. *J. Phys. Chem.* **1971**, *75* (8), 991−1024.
(29) Berlman, I. B. *Handbook of Fluorescence Spectra of Aromatic Molecules*, 2d ed.; Academic Press: New York and London: N.Y., 1971.
(30) Gehman, V. M.; Seibert, S. R.; Rielage, K.; Hime, A.; Sun, Y.; Mei, D. M.; Maassen, J.; Moore, D. Fluorescence Efficiency and Visible Re-Emission Spectrum of Tetraphenyl Butadiene Films at Extreme Ultraviolet Wavelengths. *Nucl. Instrum. Methods Phys. Res., Sect. A* **2011**, *654* (1), 116−121.
(31) Francini, R.; Montereali, R. M.; Nichelatti, E.; Vincenti, M. A.; Canci, N.; Segreto, E.; Cavanna, F.; Pompeo, F. D.; Carbonara, F.; Fiorillo, G.; Perfetto, F. VUV-Vis Optical Characterization of Tetraphenyl-Butadiene Films on Glass and Specular Reflector Substrates from Room to Liquid Argon Temperature. *J. Instrum.* **2013**, *8* (09), P09006.
(32) Neese, F.; Wennmohs, F.; Becker, U.; Riplinger, C. The ORCA Quantum Chemistry Program Package. *J. Chem. Phys.* **2020**, *152* (22), 1−18.
(33) Adamo, C.; Barone, V. Toward Reliable Density Functional Methods without Adjustable Parameters: The PBE0Model. *J. Chem. Phys.* **1999**, *110* (13), 6158−6170.
(34) Hehre, W. J.; Ditchfield, R.; Pople, J. A. Self-Consistent Molecular Orbital Methods. XII. Further Extensions of Gaussian-Type Basis Sets for Use in Molecular Orbital Studies of Organic Molecules. *J. Chem. Phys.* **1972**, *56* (5), 2257−2261.
(35) Francl, M. M.; Pietro, W. J.; Hehre, W. J.; Binkley, J. S.; Gordon, M. S.; DeFrees, D. J.; Pople, J. A. Self-Consistent Molecular Orbital Methods. XXIII. A Polarization-Type Basis Set for Second-Row Elements. *J. Chem. Phys.* **1982**, *77* (7), 3654−3665.
(36) Li, R.; Zhang, X.; Dong, H.; Li, Q.; Shuai, Z.; Hu, W. Gibbs-Curie-Wulff Theorem in Organic Materials: A Case Study on the Relationship between Surface Energy and Crystal Growth. *Adv. Mater.* **2016**, *28* (8), 1697−1702.
(37) Liptay, W. Die Lösungsmittelabhängigkeit Der Wellenzahl von Elektronenbanden Und Die Chemisch-Physikalischen Grundlagen. *Z. Naturforsch., A: Phys. Sci.* **1965**, *20* (11), 1441−1471.
(38) Liptay, W. *Excited States*; Lim, E. C., Ed.; Academic Press: New York, 1974; Vol. *1,2*.
(39) Mataga, N.; Kaifu, Y.; Koizumi, M. Solvent Effects upon Fluorescence Spectra and the Dipolemoments of Excited Molecules. *Bull. Chem. Soc. Jpn.* **1956**, *29* (4), 465−470.
(40) Lippert, E. Spektroskopische Bestimmung Des Dipolmomentes Aromatischer Verbindungen Im Ersten Angeregten Singulettzustand. *Z. Elektrochem.* **1957**, *61* (8), 962−975.
(41) McRae, E. G. Theory of Solvent Effects on Molecular Electronic Spectra. Frequency Shifts. *J. Phys. Chem.* **1957**, *61* (5), 562−572.

https://doi.org/10.1021/acsomega.3c08543
ACS Omega 2024, 9, 14932−14946

(42) Birks, J. B.; Dyson, D. J. The Relations between the Fluorescence and Absorption Properties of Organic Molecules. *Proc. R. Soc. London, Ser. A* **1963**, *275* (1360), 135−148.
(43) Staab, H. A.; Kuhn, R. J. *Einführung in Die Theoretische Organische Chemie*; Verlag Chemie: Weinheim, 1959.
(44) Agranovich, V. *Excitations in Organic Solids*; Oxford Press, 2009..
(45) Davydov, A. S. *Theory of Molecular Excitons*; Plenum Press: N.Y., 1971..
(46) Davydov, A. S. *Theory of Molecular Exitons*; Mc Grow—Hill Company: New York, 1962.
(47) *Solvatochromism: Problems and Methods*, Bakhshiev, N. G., Ed.; Leningr. Gos. Univ.: Leningrad, 1979.

https://doi.org/10.1021/acsomega.3c08543
ACS Omega 2024, 9, 14932−14946